Coherent Coupled Qubits for Quantum Annealing

Steven J. Weber,[1,*] Gabriel O. Samach,[1] David Hover,[1] Simon Gustavsson,[2] David K. Kim,[1] Alexander Melville,[1] Danna Rosenberg,[1] Adam P. Sears,[1] Fei Yan,[2] Jonilyn L. Yoder,[1] William D. Oliver,[1,2,3,†] and Andrew J. Kerman[1,‡]

[1]*MIT Lincoln Laboratory, 244 Wood Street, Lexington, Massachusetts 02420, USA*

[2]*Research Laboratory of Electronics, Massachusetts Institute of Technology, Cambridge, Massachusetts 02139, USA*

[3]*Department of Physics, Massachusetts Institute of Technology, Cambridge, Massachusetts 02139, USA*

(Received 23 January 2017; revised manuscript received 14 April 2017; published 10 July 2017)

Quantum annealing is an optimization technique which potentially leverages quantum tunneling to enhance computational performance. Existing quantum annealers use superconducting flux qubits with short coherence times limited primarily by the use of large persistent currents I_p. Here, we examine an alternative approach using qubits with smaller I_p and longer coherence times. We demonstrate tunable coupling, a basic building block for quantum annealing, between two flux qubits with small (approximately 50-nA) persistent currents. Furthermore, we characterize qubit coherence as a function of coupler setting and investigate the effect of flux noise in the coupler loop on qubit coherence. Our results provide insight into the available design space for next-generation quantum annealers with improved coherence.

DOI: 10.1103/PhysRevApplied.8.014004

I. INTRODUCTION

Quantum annealing [1–4] is a heuristic technique for finding the low-energy configurations of complicated Ising models. It has received considerable interest as a potential new computing paradigm for solving classical optimization problems [5], which are important for a wide range of applications in science and industry. Existing quantum annealers, despite rapid progress in system size and intensive efforts to benchmark performance, have yet to demonstrate improved scaling over classical methods [6–14]. While continued efforts to scale and improve existing quantum-annealing architectures will provide a clearer picture of their potential capabilities, it is also worthwhile to consider their limitations and explore alternative approaches which may be more amenable to quantum-enhanced performance.

Commercial quantum annealers developed by D-Wave Systems are based on niobium flux qubits with relatively short coherence times and are designed to implement stoquastic Hamiltonians [15] with pairwise Ising couplings limited to a "Chimera" connectivity graph [16,17]. Experience with the D-Wave platform suggests that it could benefit from higher connectivity, increased precision in setting parameters, and greater control over the annealing schedule. In addition, increased qubit coherence, non-stoquastic Hamiltonians, and multiqubit interactions [18] may also be instrumental in achieving quantum-enhanced performance. In this work, we focus on the challenge of improving the coherence of coupled qubits in a quantum annealer.

Superconducting flux qubits [19,20] are well suited to quantum annealing because they can be used to approximately realize the transverse Ising model Hamiltonian $\hat{H}_I = (\hbar/2)\sum_i(\epsilon_i\hat{\sigma}_i^z + \Delta_i\hat{\sigma}_i^x) + \sum_{i<j}\hbar J_{ij}\hat{\sigma}_i^z\hat{\sigma}_j^z$, where $\hbar\epsilon_i$ and $\hbar\Delta_i$ play the roles of the Zeeman energies due to the z and x components of the local field seen by the ith spin, and J_{ij} is the Ising interaction between spins i and j. Here, the two eigenstates of the Pauli operator $\hat{\sigma}_i^z$ correspond to "persistent-current" states of qubit i, which can be viewed as clockwise and counterclockwise currents of magnitude I_p circulating around the qubit loop. For a quantum-annealing device based on the transverse Ising model, the parameters ϵ_i and J_{ij} are used to encode a classical problem, while nonzero Δ_i are the source of the quantum fluctuations which drive the annealing process. In general, all of these parameters must be tunable. In a flux-qubit-based implementation, a coupler mediates an interaction between qubits i and j, and the parameters ϵ_i, Δ_i, and J_{ij} are tunable via local magnetic flux biases.

The coupler elements [18,19,21–31] are themselves also flux qubits, though operated in a regime where they can be described as a simple flux-tunable effective inductance L_{eff}. In this language, the coupling energy between two qubits, each with persistent current I_p and mutual inductance M with the coupler, is given by $J = I_p^2M^2/L_{\text{eff}}$. The quantity $1/L_{\text{eff}}$ is also referred to as the coupler susceptibility [28].

The most significant design parameter to affect the coherence of a quantum annealer is the choice of I_p. Flux qubits with large persistent current have a naturally strong coupling as $J \propto I_p^2$, but their coherence times are

*steven.weber@ll.mit.edu
†oliver@ll.mit.edu
‡ajkerman@ll.mit.edu

severely limited by flux noise: their sensitivity to flux noise is proportional to I_p and can limit both the energy-relaxation time and the dephasing time [32,33], which for $1/f$ flux noise roughly scale as $1/I_p^2$ and $1/I_p$, respectively. In the D-Wave system, the qubits are designed with large persistent currents $I_p \sim 3\ \mu$A [16] in order to achieve large coupling strength with modest values of coupler susceptibility and M. In contrast, we recently demonstrated that it is possible to produce robust, long-lived flux qubits with small persistent currents $I_p \sim 50$ nA [32]. In order to realize strong coupling between qubits with small I_p, it is necessary to compensate by increasing either M or the coupler susceptibility. Although this approach increases the qubit's sensitivity to flux noise in the coupler loop and requires more precise control over the coupler flux bias, it nevertheless allows for a significant improvement in qubit coherence.

In this work, we demonstrate tunable coupling between qubits with persistent currents reduced by nearly 2 orders of magnitude compared to existing quantum annealers. While coupled flux qubits with low persistent currents have been previously demonstrated [24], no work to date has investigated the implications that this design choice has on qubit coherence for quantum annealing. We present a systematic study of the coherence of coupled flux qubits in the context of quantum annealing. In particular, we investigate the effect of flux noise in the coupler loop on qubit coherence. Our results are in good agreement with simulations based on the full Hamiltonian of the coupled-qubit system, as well as a semiclassical model. This work serves as a proof of principle and provides a framework for evaluating coherence in future quantum-annealing architectures.

II. EXPERIMENTAL SETUP

A circuit diagram of our coupled-qubit device is shown in Fig. 1(a). Two capacitively shunted three-junction flux qubits, qubit A and qubit B, are each galvanically coupled to a rf-superconducting quantum-interference-device (rf-SQUID) coupler via a shared inductance of $M = 34$ pH, as shown in Figs. 1(b)–1(d). The devices are controlled by the externally applied magnetic fluxes Φ_A, Φ_B, and Φ_C. For simplicity, our experiments use qubits with a single superconducting loop instead of the multiloop qubits that are required for independent Δ tunability. We characterize the qubits using standard dispersive measurements [34], with each qubit coupled to a separate readout resonator which is probed through a shared transmission line.

The transition frequency between the coupler ground and first excited state $\omega_C^{01}/2\pi$ is designed to be approximately 20 GHz, which is significantly larger than the qubit transition frequencies at approximately 5 GHz. Therefore, the coupled-qubit system can be described by

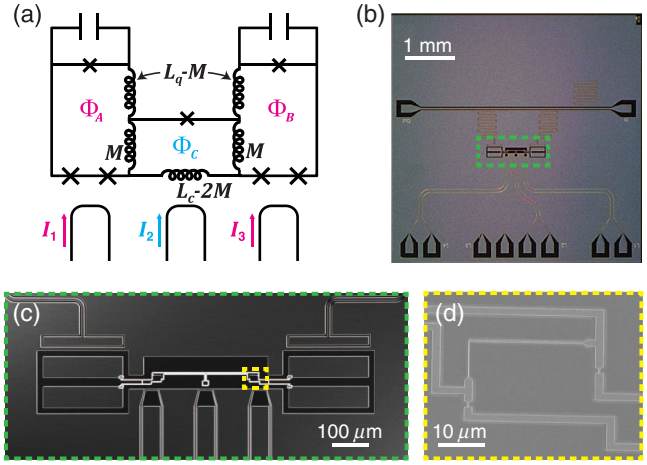

FIG. 1. Coupled-qubit geometry. (a) Device schematic. Qubit A (left loop) and qubit B (right loop) are capacitively shunted three-junction flux qubits coupled through a shared inductance with a rf-SQUID coupler (center loop). On-chip bias currents I_1, I_2, and I_3 control the external fluxes Φ_A, Φ_C, and Φ_B through the qubit and coupler loops. (b) Optical micrograph of the aluminum (light gray) device on a silicon (dark gray) substrate. (c) Optical image showing the qubits, coupler, and flux bias lines. (d) SEM image of the galvanic connection between qubit B (lower right) and the coupler (upper left).

the approximate low-energy Hamiltonian $H \approx H_q^{(A)} + H_q^{(B)} + H_{\rm int}$ [26], where

$$H_q^{(i)} = \frac{\hbar}{2}[\epsilon_i(\Phi_{A,B,C})\hat{\sigma}_z^{(i)} + \Delta_i(\Phi_{A,B,C})\hat{\sigma}_x^{(i)}], \quad (1)$$

$$H_{\rm int} = \hbar J(\Phi_{A,B,C})\sigma_z^{(A)}\sigma_z^{(B)}. \quad (2)$$

The effective parameters ϵ_i, Δ_i, and J are determined not only by the circuit parameters of the individual qubits and coupler but also by their couplings and can depend on all three flux biases. For each qubit, the degeneracy point is defined as the bias where $\epsilon_i = 0$. A table of device parameters can be found in Appendix A.

The qubits are designed with shunt capacitance $C_{\rm sh} = 50$ fF, loop inductance $L_q = 110$ pH, and $I_p = 45$ nA. All device components are patterned from a high-quality evaporated aluminum film on a high-resistivity silicon wafer, except for the superconducting loops and Josephson junctions, which are deposited using double-angle evaporation of aluminum [32]. Spectroscopy plots showing the energy difference between the ground and first excited state for qubit A and qubit B are shown in Figs. 2(a) and 2(b) as a function of the reduced flux $f_i \equiv \Phi_i/\Phi_0$ in the qubit loop, with the coupler biased at $f_C = 0$. At this coupler bias, $\Delta_A/2\pi = 5.042$ GHz and $\Delta_B/2\pi = 5.145$ GHz.

Figure 2(c) shows how the transition frequency of qubit B depends on the coupler bias. This dependence originates

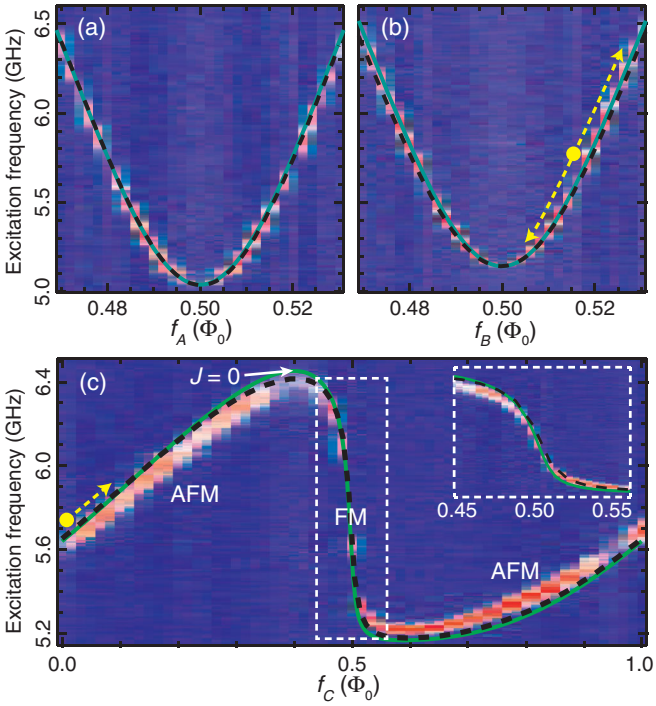

FIG. 2. Qubit spectroscopy. Dashed black traces: Semiclassical model. Solid green traces: Simulations of the full-circuit Hamiltonian. (a) Spectroscopy of qubit A vs f_A, with $f_B = f_C = 0$. (b) Spectroscopy of qubit B vs f_B with $f_A = f_C = 0$. The yellow dashed line represents the starting point and range of qubit frequencies in the following panel. (c) Spectroscopy of qubit B vs f_C for $f_A = 0$ and $f_B = 0.516$. The regions of antiferromagnetic (AFM), ferromagnetic (FM), and zero coupling are indicated. The inset shows detailed data for the FM region.

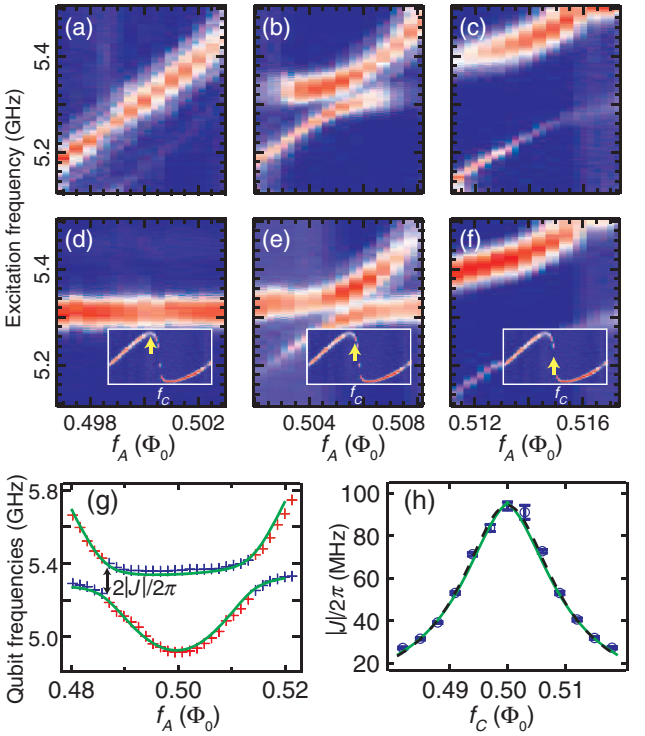

FIG. 3. Qubit-qubit coupling. Dashed black traces: Semiclassical model. Solid green traces: Simulations of the full-circuit Hamiltonian. (a)–(f) Spectroscopy of qubit-level crossings for different coupling strengths. Panels (a)–(c) and (d)–(f) show measurements using resonator A and resonator B, respectively. In each panel, we scan f_A while holding f_B at a fixed bias point approximately 10 mΦ_0 away from degeneracy. The left, middle, and right panels correspond to zero ($f_C = 0.402$), intermediate ($f_C = 0.48$), and maximum ($f_C = 0.5$) coupling, as indicated by the insets. (g) Avoided level crossings as qubit A (red) is tuned across qubit B (blue) with $f_C = 0.5$. (h) J vs coupler bias. Error bars are derived from the error of fitting the qubit spectroscopy to a double Gaussian function.

from the circulating current in the coupler loop $\langle I^C \rangle$, which couples to the qubit through the shared inductance M. Thus, the coupler induces an offset flux in the qubit loop, which shifts the effective qubit bias as indicated by the dashed line in Fig. 2(b). Treating the interaction classically, the offset flux is given by $\delta f_B = M\langle I^C \rangle/\Phi_0$. Assuming that the coupler remains in its ground state, $\langle I^C \rangle$ and L_{eff} are related to the coupler ground-state energy $E_0^{(C)}$ as

$$\langle I^C \rangle \equiv \frac{\partial E_0^{(C)}}{\partial \Phi_C}; \qquad \frac{1}{L_{\text{eff}}} \equiv \frac{\partial \langle I^C \rangle}{\partial \Phi_C} = \frac{\partial^2 E_0^{(C)}}{\partial \Phi_C^2}. \tag{3}$$

By fitting our results to theory, we extract the rf-SQUID coupler loop inductance $L_C = 470$ pH and junction critical current $I_C^0 = 730$ nA, giving $\beta \equiv 2\pi L_C I_C^0/\Phi_0 = 1.04$. $\langle I^C \rangle$ and $1/L_{\text{eff}}$ vary with f_C, and for these coupler parameters, they range from -700 to 700 nA and $1/(1070\ \text{pH})$ to $1/(-48\ \text{pH})$, respectively. Note that the slope of $\langle I^C \rangle$ with respect to flux determines the sign of L_{eff} and, thus, the sign of J. Therefore, Fig. 2(c) can be seen as a map of the regions of antiferromagnetic ($J > 0$), ferromagnetic ($J < 0$), and zero coupling.

III. COUPLING STRENGTH

Two-qubit coupling is shown in Fig. 3 focusing primarily on the ferromagnetic coupling regime. Figures 3(a)–3(f) show spectroscopy of both qubits as the transition frequency of qubit A is tuned through resonance with that of qubit B, which is held at a fixed bias. When the qubits are resonant, their levels hybridize and split in frequency by $2|J|$, shown here for three coupler biases corresponding to different values of coupling strength J. Figure 3(g) shows the qubit frequencies for maximal coupling, as f_A is tuned over a much larger range. At this coupler bias, we measure a maximal coupling strength of $|J|/2\pi = 94$ MHz. From this measurement and our experimental bound on the minimum coupling (see Appendix E), we place a lower bound of 425 on the coupler on:off ratio. Finally, Fig. 3(h) shows the dependence of $|J|$ on the coupler bias, which agrees well with simulations of the full-circuit Hamiltonian, as well as a semiclassical model (see Appendix B).

IV. QUBIT COHERENCE

In Fig. 4, we show how the properties of an individual qubit depend on the coupler bias. Here, we present data for qubit B, with f_A set to zero. Figures 4(a) and 4(b) display Δ_B versus f_C. For each value of f_C, we sweep f_B and perform qubit spectroscopy to find the minimum qubit frequency, $\omega_B^{\min}(f_C) \equiv \Delta_B(f_C)$. The dependence of Δ_B on f_C can be understood semiclassically as loading of the qubit inductance by the effective inductance of the coupler,

$$L_q^{\text{loaded}} = L_q - \frac{M^2}{L_{\text{eff}}}, \tag{4}$$

as illustrated by the dashed lines in Figs. 4(a) and 4(b).

In Figs. 4(c) and 4(d), we show how the qubit energy-relaxation time T_1 depends on f_C. For each coupler bias point, qubit B is biased on degeneracy (at the point of minimum qubit frequency). The error bars correspond to the standard error for fitting the decay curve at each coupler bias point to an exponential function. In addition to any dependence on the coupler bias, T_1 also fluctuates on slow time scales [32,35], and the gray band indicates the typical range of T_1 fluctuations when the coupler is biased away from degeneracy (see Appendix D). When the coupler is biased near degeneracy, we observe a reduction in T_1 substantially below the range of temporal fluctuations.

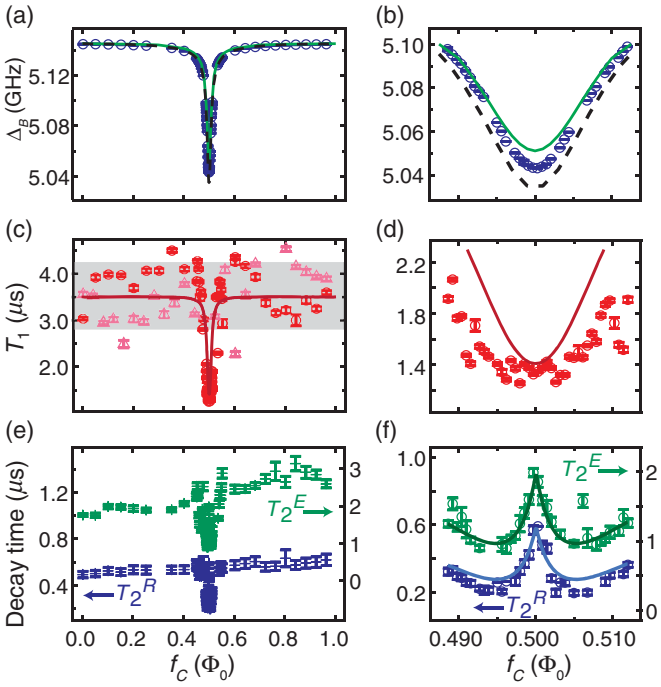

FIG. 4. Qubit properties vs coupler bias. Results for qubit B, with $f_A = 0$. Left column: Full range of coupler biases. Right column: Enlargement of the region near coupler degeneracy. (a), (b) Δ_B vs coupler bias. Dashed black traces: Semiclassical model. Solid green traces: Simulations of the full-circuit Hamiltonian. (c),(d) Qubit energy-relaxation time vs coupler bias. The red circles and the magenta triangles correspond to measurements taken at different times. The gray band indicates the typical range of T_1 variations when the coupler is biased away from degeneracy. The solid line represents an upper bound on qubit T_1 due to flux noise in the coupler loop with an exponent $\alpha = 0.91$ and an amplitude of 15 $\mu\Phi_0/\sqrt{\text{Hz}}$ combined in parallel with a coupler-independent relaxation time of 3.5 μs. (e),(f) Ramsey (left axis) and echo (right axis) $1/e$ decay times vs coupler bias. Solid lines show the expected dependence due to $1/f^{\alpha}$-flux noise in the coupler loop with the same amplitude and exponent as above.

Finally, Figs. 4(e) and 4(f) show the dependence of the qubit dephasing times on f_C, for the same bias conditions as above. Here, we report the $1/e$ decay times T_2^{Ramsey} and T_2^{echo} for Ramsey interferometry and spin-echo experiments, respectively. When the coupler is biased away from degeneracy, T_2^{Ramsey} is essentially constant with respect to f_C. There is some variation in T_2^{echo}, which is roughly consistent with the range of values expected from the observed fluctuations in T_1.

Interestingly, we observe a sharp reduction in the coherence times as the coupler bias approaches degeneracy and a full recovery when the coupler is biased exactly on degeneracy. This effect can be understood as the result of the first-order sensitivity of Δ_B to the coupler bias, which is given by $\partial\Delta_B/\partial\Phi_C$, the slope of the data in Figs. 4(a) and 4(b). By fitting the measured dependence of Δ_B on f_C and assuming a $1/f^{\alpha}$ spectral density of fluctuations with $\alpha = 0.91$ [36], we see excellent agreement between our model and the coherence measurements for a flux-noise amplitude of 15 $\mu\Phi_0/\sqrt{\text{Hz}}$, as indicated by the curves in Fig. 4(f). Using the same amplitude and exponent, we calculate an upper limit on qubit T_1 due to flux noise in the coupler loop, as shown in Figs. 4(c) and 4(d). In Appendix D, we speculate on why the estimated flux-noise amplitude is larger than the previously reported values for flux qubits made with the same fabrication process [32] and the potential implications for future quantum-annealing architectures designed to optimize for both coherence and coupling.

This work represents an important step toward designing quantum annealers with improved coherence. We demonstrate tunable coupling between flux qubits with substantially lower persistent currents than existing commercial devices, thereby reducing the qubit sensitivity to flux noise in their respective loops. This approach requires an increased coupler susceptibility, which increases the qubits' sensitivity to flux noise in the coupler loop. We examine this effect by measuring qubit coherence across the full range of coupler biases, using standard measurement techniques borrowed from the gate-based quantum-computing community, which have yet to be applied to commercial quantum annealers. Looking forward, our approach can be extended to achieve larger coupling strength, symmetric bipolar coupling, and $\hat{\sigma}_x\hat{\sigma}_x$ interactions [37], while maintaining low persistent currents. Our results provide insights into the available design space and suggest

the type of system-level analysis that is necessary when designing quantum annealers with improved coherence.

ACKNOWLEDGMENTS

We gratefully acknowledge Wayne Woods for useful discussions and P. Baldo, G. Fitch, X. Miloshi, P. Murphy, B. Osadchy, K. Parrillo, A. Sevi, and R. Slattery at MIT Lincoln Laboratory for technical assistance. This research is funded by the Office of the Director of National Intelligence (ODNI), Intelligence Advanced Research Projects Activity (IARPA), and by the Assistant Secretary of Defense for Research & Engineering under Air Force Contract No. FA8721-05-C-0002. The views and conclusions contained herein are those of the authors and should not be interpreted as necessarily representing the official policies or endorsements, either expressed or implied, of ODNI, IARPA, or the U.S. Government.

APPENDIX A: TABLE OF SAMPLE PARAMETERS

Table I shows a list of sample parameters extracted from two different models of the coupled-qubit system—a semiclassical model, where the individual qubits and coupler are treated quantum mechanically but their interactions are treated as a classical mutual inductance, and a quantum model of the full galvanically coupled circuit. Using the semiclassical model, we perform an optimization routine to determine the set of parameters which best fit the results in Figs. 2–4. The quantum model includes some effects, such as cross-capacitance between the qubits and coupler, which are not included in the semiclassical model. Therefore, it is necessary to make small adjustments to the parameters extracted from the semiclassical model in order to achieve good agreement between the quantum model and the measured results, as indicated in Table I.

TABLE I. Table of sample parameters.

	Parameter	Semiclassical model	Full galvanic circuit model
Common junction params.	J_c (μA)	2.78	2.78
	S_c (fF/μm^2)	50	50
Qubit A	$I_0^{A,\mathrm{sm}}$ (nA)	78	78
	$I_0^{A,\mathrm{lg}}$ (nA)	206	206
	C_{sh}^A (fF)	53	53
	L_q^A (pH)	115	115
Qubit B	$I_0^{B,\mathrm{sm}}$ (nA)	78	78
	$I_0^{B,\mathrm{lg}}$ (nA)	209	209
	C_{sh}^B (fF)	53	53
	L_q^B (pH)	115	115
Coupling	M (pH)	39	43
	I_0^C (nA)	727	736
	L_C (pH)	467	542

APPENDIX B: SEMICLASSICAL MODEL

Figure 5 shows a circuit diagram for the full galvanically coupled circuit. To simulate the energy levels of the full system, we diagonalize the circuit Hamiltonian using similar techniques to our previous work [32]. These techniques are described in detail in a separate forthcoming publication [38].

In this section, we explain how to map the full circuit onto a simpler and more computationally convenient semiclassical model. In this model, the individual qubits and coupler are treated quantum mechanically, but their interactions are treated as a classical mutual inductance. Using this simplified model, we derive expressions for the coupling strength J, as well as the shifts in the qubit parameters Δ and ϵ due to interaction with the coupler.

1. Comparing mutually inductive coupling to galvanic coupling

To build up the model of the coupled-qubit system, we first consider a simpler system depicted in Fig. 6(a). Here, two loops of inductance $L_{A,B}$ threaded by magnetic flux $\Phi_{A,B}$ are coupled through a mutual inductance M.

Defining the flux vector $\boldsymbol{\Phi}$, the mutual inductance matrix $\boldsymbol{M}$, and the self-inductance matrix $\boldsymbol{L}$ as

$$\boldsymbol{\Phi} \equiv \begin{pmatrix} \Phi_A \\ \Phi_B \end{pmatrix}; \quad \boldsymbol{M} \equiv \begin{pmatrix} 0 & -M \\ -M & 0 \end{pmatrix}; \quad \boldsymbol{L} \equiv \begin{pmatrix} L_A & 0 \\ 0 & L_B \end{pmatrix}, \tag{B1}$$

the classical potential energy of the system is given by

$$U = \frac{1}{2}\boldsymbol{\Phi}(\boldsymbol{L}^{-1} + \boldsymbol{L}^{-1}\boldsymbol{M}\boldsymbol{L}^{-1})\boldsymbol{\Phi} \tag{B2}$$

$$= \frac{1}{2}\frac{\Phi_A^2}{L_A} + \frac{1}{2}\frac{\Phi_B^2}{L_B} + M\frac{\Phi_A}{L_A}\frac{\Phi_B}{L_B}, \tag{B3}$$

where the first two terms correspond to the energies of the individual loops, and the third term represents their interaction energy. The system can be reexpressed in terms of the classical circulating currents $I_{A,B} = \Phi_{A,B}/L_{A,B}$, which yields

$$U = \frac{1}{2}L_A I_A^2 + \frac{1}{2}L_B I_B^2 + M I_A I_B. \tag{B4}$$

Next, we compare this result for two mutually coupled loops to the case of two galvanically coupled loops, as depicted in Fig. 6(b). Here, the inductance matrix can be approximately defined as [40]

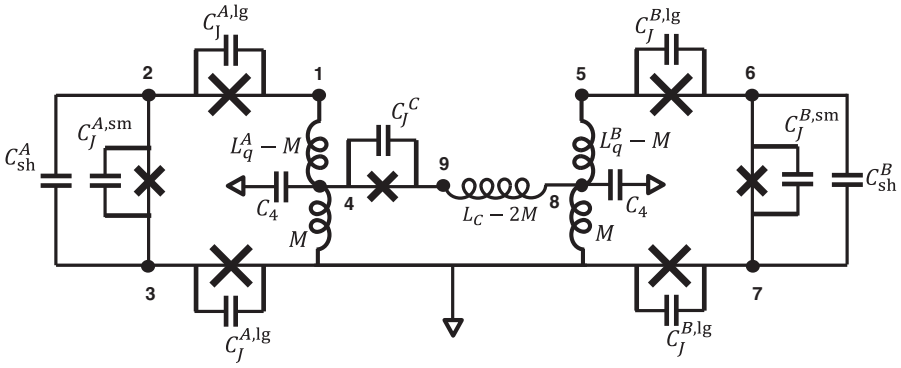

FIG. 5. Schematic diagram of the full galvanic circuit. The nodes of the circuit labeled 1–9 are used to define its canonical flux and charge variables [39].

$$\boldsymbol{L} \equiv \begin{pmatrix} L_A & -M \\ -M & L_B \end{pmatrix}, \tag{B5}$$

and the potential energy is given by

$$U = \frac{1}{2}\boldsymbol{\Phi}\boldsymbol{L}^{-1}\boldsymbol{\Phi} \tag{B6}$$

$$= \frac{1}{2}\frac{\Phi_A^2}{L_A - M^2/L_B} + \frac{\Phi_B^2}{L_B - M^2/L_B} + M\left(1 - \frac{M^2}{L_A L_B}\right)^{-1}\frac{\Phi_A}{L_A}\frac{\Phi_B}{L_B}. \tag{B7}$$

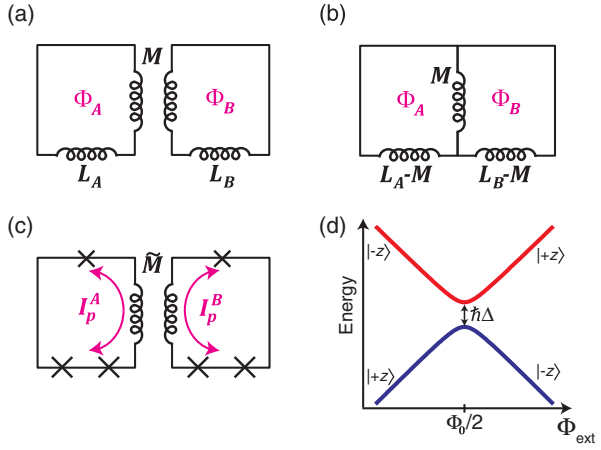

FIG. 6. Direct coupling. (a) Circuit schematic for two loops of inductance $L_{A,B}$ coupled through a mutual inductance M. (b) Circuit schematic for two loops which are galvanically coupled through a shared inductance M. (c) Circuit schematic for two flux qubits with persistent currents $I_p^{A,B}$ coupled through a mutual inductance $\tilde{M}$. (d) Illustration of the energies of the ground (blue) and first excited (red) states of a flux qubit as a function of the external flux Φ_{ext} through the qubit loop. At the degeneracy point ($\Phi_{\mathrm{ext}} = \Phi_0/2$), the ground and excited states are separated in energy by $\hbar\Delta$. When biased away from degeneracy, the qubit states are approximately persistent current states $|\pm z\rangle$.

Note that this is equivalent to Eq. (B3) after the following substitutions:

$$\tilde{L}_{A,B} \equiv L_{A,B} - \frac{M^2}{L_{B,A}}; \qquad \tilde{M} \equiv M\left(1 - \frac{M^2}{L_A L_B}\right). \tag{B8}$$

Thus, the galvanically coupled circuits employed in this work can be approximately mapped onto simpler mutually coupled circuits using the renormalized inductances $\tilde{L}$ and $\tilde{M}$.

2. Directly coupled qubits

Now, suppose that each loop in the circuits discussed above is replaced with a flux qubit [Figs. 6(c) and 6(d)] described by the Hamiltonian $H_q/\hbar \approx (\epsilon\hat{\sigma}_z + \Delta\hat{\sigma}_x)/2$. In the persistent-current basis, the eigenstates of the Pauli operator $\hat{\sigma}_z$ denoted $|\pm z\rangle$ correspond to clockwise- and counterclockwise-circulating currents

$$I \equiv \langle \pm z|\hat{I}|\pm z\rangle = \langle \pm z|I_p\hat{\sigma}_z|\pm z\rangle = \pm I_p, \tag{B9}$$

where $\hat{I}$ is the current operator, and I_p is magnitude of the qubit persistent current. The interaction term from Eq. (B4) can be expressed as

$$H_{\mathrm{int}} = \tilde{M} I_p^A I_p^B \hat{\sigma}_z^{(A)}\hat{\sigma}_z^{(B)}, \tag{B10}$$

which takes the form $H_{\mathrm{int}} = J\hat{\sigma}_z^{(A)}\hat{\sigma}_z^{(B)}$, where the coupling strength J is given by

$$\hbar J = \tilde{M} I_p^A I_p^B. \tag{B11}$$

A simple intuitive picture for this expression emerges when the qubits are biased such that $\epsilon \gg \Delta$. In this regime, qubit energy eigenstates are approximately equal to the persistent current states $|\pm z\rangle$ with energy eigenvalues $\pm\hbar\epsilon/2 = I_p(\Phi_{\mathrm{ext}} - \Phi_0/2)$, where Φ_{ext} is the external magnetic flux through the qubit loop, and Φ_0 is the magnetic flux quantum. Here, the $\hat{\sigma}_z\hat{\sigma}_z$ interaction is longitudinal with respect to the energy eigenbasis. The coupling can be

understood by considering the effect of the persistent current in one qubit loop on the flux through the other qubit loop. For example, qubit A induces a state-dependent offset $\delta\Phi_B = \pm\tilde{M}I_p^A$ in the flux through qubit B and, thus, a state-dependent frequency shift of

$$\delta\omega_{01}^{(B)} \approx \pm\epsilon\delta\Phi_B = \pm 2J. \tag{B12}$$

Note that the coupling measurements reported in the main text are performed in the $\Delta \gg \epsilon$ regime, where the $\hat{\sigma}_z\hat{\sigma}_z$ interaction is transverse with respect to the energy eigenbasis. In this case, the coupling manifests as an avoided crossing between the $|01\rangle$ and $|10\rangle$ states, which are shifted from their bare energies by $\pm\hbar J$.

3. Mediated coupling

As a next step in building up the semiclassical coupling model, we consider the case of two qubits coupled through a mutual inductance $\tilde{M}$ to an intermediate loop of inductance L [Fig. 7(a)]. Returning to the longitudinal coupling picture ($\epsilon \gg \Delta$), the persistent current in qubit A induces a state-dependent offset flux $\delta\Phi_C = \pm\tilde{M}I_p^A$ in the coupler loop, which changes the current circulating in the loop by $\delta\langle I^C\rangle = \delta\Phi_C/L$ and, thus, induces an offset of

$$\delta\Phi_B = \delta\Phi_C\frac{\tilde{M}}{L} = \frac{\tilde{M}^2}{L}I_p^A \tag{B13}$$

in the flux through qubit B. Note that this expression takes the same form as for the directly coupled qubits but with the substitution $\tilde{M} \to \tilde{M}^2/L \equiv M_{\text{eff}}$. Then, in analogy to Eq. (B11), the coupling strength is given by

$$J = \frac{\tilde{M}^2}{L}I_p^A I_p^B = M_{\text{eff}}I_p^A I_p^B. \tag{B14}$$

Finally, we consider the case where the intermediate loop is replaced with a rf-SQUID coupler [Fig. 7(b)]. In the following discussion, we make the assumption that transition frequency between the coupler ground and first excited state is much larger than the qubit frequencies and that the coupler is always operated in its ground state. In general, the coupler ground-state energy E_0 varies with applied flux f_C, as illustrated in Fig. 7(c). For the coupler parameters considered in this work, the circulating current in the coupler loop is approximately equal to the slope of the coupler energy with respect to the flux $\langle I^C\rangle \approx \partial E_0^C/\partial\Phi_C$, as illustrated in Fig. 7(d), where we compare this quantity with the expectation value of the current operator $\langle g|\hat{I}|g\rangle$ for the coupler ground state $|g\rangle$.

We then define the "quantum inductance" for the coupler (as in Refs. [28,41,42] and in analogy to the "quantum capacitance" described in the charge qubit [41,43,44] and semiconducting qubit [45–50] literature) as

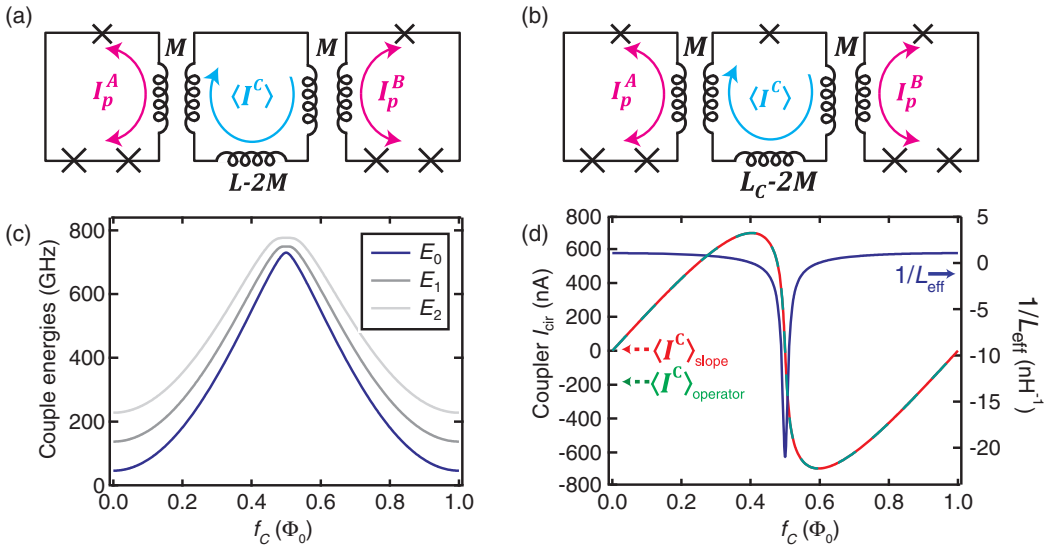

FIG. 7. Mediated coupling. (a) Circuit schematic for two flux qubits with persistent currents $I_p^{A,B}$ which each couple through a mutual inductance $\tilde{M}$ to an intermediate loop of inductance L. (b) Circuit schematic for a similar configuration but with the intermediate loop replaced with a rf-SQUID coupler. (c) Illustration of the energies of the ground (blue) and first excited (gray) states of a rf-SQUID coupler as a function of the external flux Φ_c through the coupler loop. (d) Left axis: Comparison of the coupler circulating current calculated using the slope of the ground-state energy (red) and using the current operator (green). Right axis: Effective inductance of the coupler vs Φ_c.

$$\frac{1}{L_{\text{eff}}} \equiv \frac{\partial \langle I^C \rangle}{\partial \Phi_C} \approx \frac{\partial^2 E_0^{(C)}}{\partial \Phi_C^2}. \tag{B15}$$

Note that unlike a physical inductance, this quantum inductance can take both positive and negative values. Following the same logic as above, we can now express the coupling strength as

$$J = \frac{\tilde{M}^2}{L_{\text{eff}}} I_p^A I_p^B. \tag{B16}$$

Given a set of qubit and coupler parameters, it is straightforward to calculate J using Eq. (B16). We determine L_{eff} by numerically diagonalizing the coupler Hamiltonian to solve for its ground-state energy E_0 as a function of Φ_C. We separately determine I_p by numerically solving for the energy eigenstates $|\psi_j\rangle$ of the qubit Hamiltonian, from which we calculate the matrix elements of the current operator $\langle \psi_j | \hat{I} | \psi_k \rangle$ expressed in the energy eigenbasis. When the qubit is biased on degeneracy ($\epsilon = 0$), the I_p is given by the off-diagonal matrix elements.

Note that Eq. (B16) is the same expression for the coupling strength used by D-Wave in Refs. [26,28], with the coupler susceptibility χ defined as the inverse of the effective inductance. However, their approach differs in that instead of diagnolizing the coupler Hamiltonian to solve for χ, D-Wave chooses to approximate χ as the first-order (linear) susceptibility, which can be expressed using a simple analytic formula. This approach works sufficiently well for the coupler parameters of existing D-Wave devices, but the linear approximation breaks down for larger coupler susceptibilities and coupling strengths, as discussed in Ref. [18].

4. Qubit flux offset due to the coupler

The semiclassical model can also explain the shifts in qubit parameters due to their interaction with the coupler. For concreteness and to follow the presentation of the main text, we focus on qubit B. First, we consider the effect of the coupler on the qubit flux bias. This effect explains the dependence of the qubit frequency on the coupler bias shown in Fig. 2(c).

As shown in Fig. 7(d), the circulating current in the coupler loop $\langle I^C \rangle$ varies with the coupler bias Φ_C. This circulating current couples into the qubit loop through the mutual inductance M and, therefore, threads a flux

$$\delta \Phi_B = \tilde{M} \langle I^C \rangle \tag{B17}$$

through the qubit loop. For a flux qubit described by the Hamiltonian $H_q/\hbar \approx (\epsilon \hat{\sigma}_z + \Delta \hat{\sigma}_x)/2$, this flux offset corresponds to a shift in ϵ of

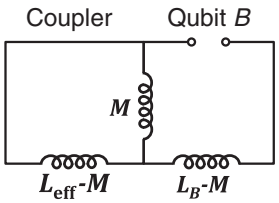

FIG. 8. Inductive loading model. Circuit schematic used to model the loading of the qubit inductance due to the coupler L_{eff}.

$$\delta \epsilon = \frac{2}{\hbar} I_p \delta \Phi_B = \frac{2}{\hbar} \tilde{M} I_p \langle I^C \rangle. \tag{B18}$$

5. Inductive loading model

The coupler also affects the value of Δ, the qubit frequency when biased at its degeneracy point, as shown for qubit B in Figs. 4(a) and 4(b). This effect can be modeled semiclassically as inductive loading of the qubit inductance by the effective inductance of the coupler.

A circuit schematic for the inductive loading model is shown in Fig. 8 [51]. Here, we consider the impedance looking out from the Josephson junction to calculate loaded qubit inductance

$$\begin{aligned} L_B^{\text{loaded}} &= L_B - M + \left(\frac{1}{L_{\text{eff}} - M} + \frac{1}{M} \right)^{-1} \\ &= L_B - \frac{M^2}{L_{\text{eff}}}. \end{aligned} \tag{B19}$$

Note that this expression for the loaded inductance is the same as the renormalized inductance derived in Eq. (B8). To calculate the semiclassical theory curves for Δ_B versus f_C [Figs. 4(a) and 4(b)], we first simulate the coupler to determine $L_{\text{eff}}(f_C)$ [Fig. 7(d)]. Then, for each value of f_C, we determine Δ_B by simulating the qubit energy levels using L_B^{loaded} for the qubit loop inductance.

APPENDIX C: VARIATIONS OF T_1 IN TIME

In addition to any systematic dependence of T_1 on the qubit and coupler biases, we also observe T_1 variations in time. These variations are possibly related to quasiparticle fluctuations, as described in Ref. [35]. Although T_1 fluctuations are not a primary focus of this work, they affect the interpretation of the data shown in Figs. 4(c) and 4(d). In Fig. 9, we show the results of repeated T_1 measurements for qubit B, with the coupler biased away from degeneracy. The range of observed T_1 values over the 14-h measurement time is represented as a gray band in Fig. 4(c).

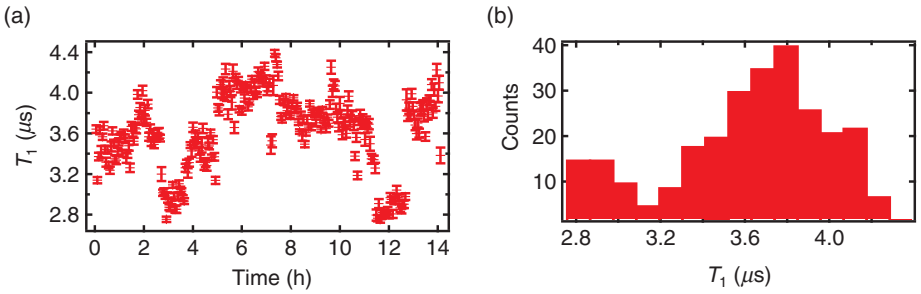

FIG. 9. Repeated T_1 measurements. (a) Repeated measurements of T_1 of qubit B as a function of time. Here, $f_A = 0$, $f_B = 0.5$, and $f_C = 0$. (b) Histogram of measured T_1 values.

APPENDIX D: MODELING THE EFFECT OF FLUX NOISE ON QUBIT COHERENCE

1. Definition of noise spectral density

In this work, as in Ref. [32], we choose to characterize noise by the symmetric power spectral density

$$S_\lambda(\omega) = \int_{-\infty}^{\infty} d\tau \exp(-i\omega\tau)\frac{1}{2}\langle\hat{\lambda}(0)\hat{\lambda}(\tau) + \hat{\lambda}(\tau)\hat{\lambda}(0)\rangle, \quad \text{(D1)}$$

where $\hat{\lambda}$ is an operator representing a fluctuating parameter λ. The two dominant noise mechanisms for the coupled-qubit system presented here are flux noise in the qubit loop and the coupler loop $\lambda_i = \Phi_B, \Phi_C$. For $1/f$-like noise, the noise amplitude A_λ is given by [52]

$$S_\lambda(\omega) = A_\lambda^2\left(\frac{2\pi \times 1\ \text{Hz}}{\omega}\right)^\gamma, \quad \text{(D2)}$$

where $\gamma \sim 1$.

2. Energy-relaxation due to $1/f^\gamma$-flux noise

We analyze the data for T_1 of our qubit-coupler system using the Fermi golden rule model presented in Ref. [32],

$$\frac{1}{T_1} = \sum_\lambda 2\frac{|\langle e|\hat{D}_\lambda|g\rangle|^2}{\hbar^2}S_\lambda(\omega), \quad \text{(D3)}$$

where the sum is taken over decay mechanisms, $S_\lambda(\omega)$ is the power spectral density of the noise responsible for each decay mechanism, and the operator $\hat{D}_\lambda$ is the transition dipole moment which couples our system to each noise source.

For the coupled system considered here, T_1 can be decomposed into contributions from the qubit T_1^Q and the coupler T_1^C, where

$$\frac{1}{T_1} = \frac{1}{T_1^Q} + \frac{1}{T_1^C}. \quad \text{(D4)}$$

The qubit contribution dominates away from the coupler degeneracy, and both processes contribute when the system is biased near the coupler degeneracy.

In our analysis, we assume that the coupler is flux noise limited on its degeneracy, and its decay rate is, thus, given by

$$\frac{1}{T_1^C} = 2\frac{|\langle e|\hat{I}^C|g\rangle|^2}{\hbar^2}S_{\Phi_C}(\omega), \quad \text{(D5)}$$

where $|g\rangle$ and $|e\rangle$ are the ground and first excited state of the coupled system

$$\hat{H} = \hat{H}^Q + \hat{H}^C + M\hat{I}^Q\hat{I}^C. \quad \text{(D6)}$$

The quantum operators $\hat{H}^C$ and $\hat{I}^C$ ($\hat{H}^Q$ and $\hat{I}^Q$) are the Hamiltonian and loop current operator of the bare coupler (qubit), respectively, and the exact value of the matrix element $\langle e|\hat{I}^C|g\rangle$ can, thus, be calculated from the device parameters listed in Appendix A and the full quantum model of the bare qubit and coupler. As described in Appendix E, the amplitude and exponent of the flux-noise power spectral density in our coupler loop are then chosen to fit the measured values of T_1, T_2^{Ramsey}, and T_2^{echo} on coupler degeneracy.

3. First-order sensitivity to flux noise

The sensitivity κ_λ of the qubit frequency to a parameter λ determines the effect of fluctuations in λ on qubit dephasing. In the two-level approximation of the flux qubit, the qubit transition frequency is given by $\omega_{01} \approx \sqrt{\epsilon^2 + \Delta^2}$, and, to first order,

$$\kappa_\lambda \equiv \frac{\partial\omega_{01}}{\partial\lambda} \approx \frac{\partial\omega_{01}}{\partial\epsilon}\frac{\partial\epsilon}{\partial\lambda} + \frac{\partial\omega_{01}}{\partial\Delta}\frac{\partial\Delta}{\partial\lambda} = \frac{\epsilon}{\omega_{01}}\kappa_{\epsilon,\lambda} + \frac{\Delta}{\omega_{01}}\kappa_{\Delta,\lambda}, \quad \text{(D7)}$$

where $\kappa_{\epsilon,\lambda} \equiv \partial\epsilon/\partial\lambda$ and $\kappa_{\Delta,\lambda} \equiv \partial\Delta/\partial\lambda$.

In the measurements presented in Fig. 4, we characterize the coherence of qubit B when biased near its degeneracy point ($\epsilon_B = 0$). At this bias point, $\kappa_{\epsilon_B,\Phi_B}$ and $\kappa_{\epsilon_B,\Phi_C}$ are zero. Since Δ_B depends only weakly on Φ_B, the dominant first-order noise mechanism is κ_{Δ_B,Φ_C}, the sensitivity of Δ_B to the coupler flux.

4. Decoherence due to $1/f^{\gamma}$-flux noise

Here, we consider the effect of $1/f$-like flux noise, as defined in Eq. (D2), on qubit coherence. In general, this type of noise causes phase decay of the form $\exp[-\chi_N(t)]$, where [53]

$$\chi_N(\tau) = \frac{1}{2\pi}\tau^2 \sum_{\lambda} \kappa_\lambda^2 \int_0^\infty d\omega S_\lambda(\omega) g_N(\omega,\tau), \quad \text{(D8)}$$

where τ is the free evolution time, and g_N is a filter function which depends on the qubit pulse sequence. For the Ramsey ($N=0$) and Hanh echo sequences ($N=1$) considered in this work,

$$g_0(\omega,\tau) \equiv g_0(\omega\tau) = \left(\frac{\sin(\omega\tau/2)}{(\omega\tau/2)}\right)^2, \quad \text{(D9)}$$

$$g_1(\omega,\tau) \equiv g_1(\omega\tau) = \left(\frac{\sin(\omega\tau/4)}{(\omega\tau/4)}\right)^2 \sin^2(\omega\tau/4). \quad \text{(D10)}$$

Substituting Eq. (D2) into Eq. (D8) and making the additional substitution $\omega\tau \to z$ gives

$$\chi_N(\tau) = \frac{(2\pi \times 1\ \text{Hz})^\gamma}{2\pi}\tau^{1+\gamma} \sum_{\lambda} \kappa_\lambda^2 A_\lambda^2 \int_0^\infty \frac{dz}{z^\gamma} g_N(z), \quad \text{(D11)}$$

where we assume that the fluctuations in each parameter λ share a common noise exponent γ.

We define the $1/e$ dephasing rates $\Gamma_{N,\lambda}$, for each dephasing channel as

$$\Gamma_{N,\lambda} = \left[(2\pi)^{\gamma-1}\kappa_\lambda^2 A_\lambda^2 \int_0^\infty \frac{dz}{z^\gamma} g_N(z)\right]^{1/(1+\gamma)} \equiv [\kappa_\lambda A_\lambda \eta_N^{1/2}]^{2/(1+\gamma)}, \quad \text{(D12)}$$

where the numerical factors η_0, η_1 depend on the noise exponent γ and the Ramsey and echo filter functions and are defined as

$$\eta_N = (2\pi)^{\gamma-1} \int_0^\infty \frac{dz}{z^\gamma} g_N(z). \quad \text{(D13)}$$

As discussed in Ref. [53], for the case of $\gamma = 1$, these factors are given by

$$\eta_0 \approx \ln\left(\frac{1}{\omega_{\text{low}} t}\right) \quad \text{(D14)}$$

$$\eta_1 = \ln(2), \quad \text{(D15)}$$

where ω_{low} is the lower cutoff frequency set by the total time of all experimental iterations, and t is the typical free evolution time during a single experimental iteration. Note that η_1 is completely independent of the cutoff frequency, thus, avoiding any ambiguity in choosing ω_{low} and t when analyzing the echo experiments, while η_0 varies only weakly with $\omega_{\text{low}} t$ for realistic measurement settings.

For $\gamma \neq 1$, we determine the numerical factors through numerical integration of Eq. (D13), as discussed in Ref. [54]. For the Ramsey sequence,

$$\eta_0 = (2\pi)^{\gamma-1} \int_{\omega_{\text{low}} t}^\infty \frac{dz}{z^\gamma} \left(\frac{\sin(z/2)}{z/2}\right)^2 \quad \text{(D16)}$$

and for the echo sequence,

$$\eta_1 = (2\pi)^{\gamma-1} \int_0^\infty \frac{dz}{z^\gamma} \left(\frac{\sin(z/4)}{z/4}\right)^2 \sin^2(z/4). \quad \text{(D17)}$$

Figure 10(a) shows $\sqrt{\eta_{0,1}}$ as a function of γ for $\omega_{\text{low}}/2\pi = 3$ mHz and $\tau = 200$ ns.

5. Estimating the flux-noise amplitude in the coupler loop

We now combine the results of the previous sections with our qubit coherence measurements to estimate the flux-noise amplitude and exponent in the coupler loop. We first consider the Ramsey and echo results presented in Figs. 4(e) and 4(f). We define the total $1/e$ decay rates for the Ramsey and echo experiments as $\Gamma_0 \equiv 1/T_2^{\text{Ramsey}}$ and $\Gamma_1 \equiv 1/T_2^{\text{echo}}$, respectively. We separate the decay rates into two contributions: Γ_{N,Φ_C} due to flux noise in the coupler loop and $\Gamma_{N,\text{other}}$, which includes the effect of T_1 as well as any additional dephasing.

When the coupler is biased far from degeneracy, Γ_{N,Φ_C} is negligible and, thus, $\Gamma_N = \Gamma_{N,\text{other}}$. For simplicity, we model $\Gamma_{N,\text{other}}$ as an exponential decay [55]. For arbitrary coupler bias, the total phase decay takes the form

$$\exp[-\Gamma_{N,\text{other}}\tau - (\Gamma_{N,\Phi_C}\tau)^{1+\gamma}]. \quad \text{(D18)}$$

Thus, we can determine Γ_{N,Φ_C} from the measured values of Γ_N and $\Gamma_{N,\text{other}}$ through the relation

$$\Gamma_{N,\Phi_C} = \Gamma_N \left(1 - \frac{\Gamma_{N,\text{other}}}{\Gamma_N}\right)^{1/(1+\gamma)}. \quad \text{(D19)}$$

Finally, from Eq. (D12), the spectral density of flux noise in the coupler is given by

$$A_{\Phi_C} = \kappa_{\Phi_C}^{-1} \eta_N^{-1/2} (\Gamma_{N,\Phi_C})^{(1+\gamma)/2}, \quad \text{(D20)}$$

where $\kappa_{\Phi_C} \approx \kappa_{\Delta_B,\Phi_C}$ is experimentally determined from the slope of Δ_B vs Φ_C [Figs. 4(a) and 4(b)].

In Fig. 10(b), we plot the value of A_{Φ_C} that fits best to our Ramsey and echo measurements using Eq. (D20) and to our T_1 measurements using Eq. (D5), for different values of γ. Although we are unable to choose values of A_{Φ_C} and γ that fit perfectly with all three measurements,

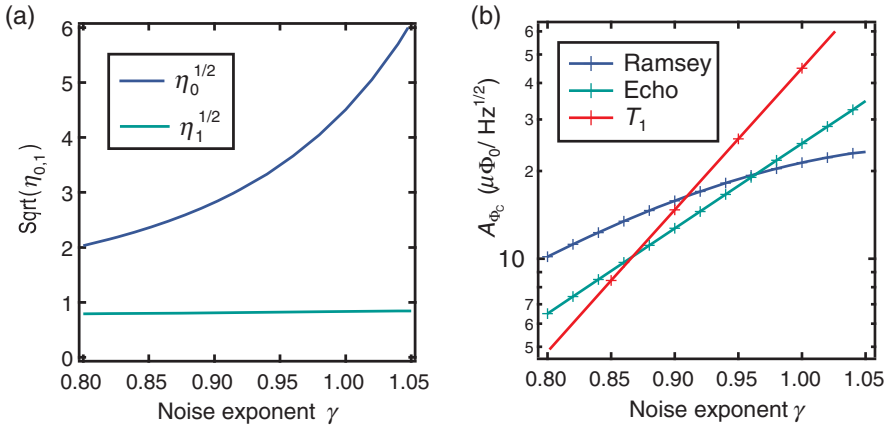

FIG. 10. Flux-noise analysis. (a) $\sqrt{\eta_{0,1}}$ vs γ determined through numerical integration. When calculating η_0, we assume $\omega_{\mathrm{low}}/2\pi = 3$ mHz and $t = 200$ ns. (b) Estimated coupler flux-noise-amplitude-based measured Ramsey, echo, and T_1 times as a function of γ.

they are roughly bounded within the triangular region between the three curves in Fig. 10(b), where $10\,\mu\Phi_0/\sqrt{\mathrm{Hz}} < A_{\Phi_C} < 19\mu\Phi_0/\sqrt{\mathrm{Hz}}$ and $0.86 < \gamma < 0.96$. For concreteness, when plotting theory curves in the main text, we choose $\gamma = 0.91$ and $A_{\Phi_C} = 15\mu\Phi_0/\sqrt{\mathrm{Hz}}$, which results in reasonably good agreement with all three measurements.

This estimate for the flux noise in the coupler loop is substantially larger than the value previously reported for flux qubits made with the same fabrication process, where we measure a flux-noise amplitude of 1.4 $\mu\Phi_0/\sqrt{\mathrm{Hz}}$ [32]. The most significant difference between the coupler loop and the low-noise qubit loops is the loop size; the coupler loop is 20 times larger in area. Therefore, these results motivate future efforts to study the dependence of flux noise on loop size beyond the scope of this work and previous efforts [56]. Such measurements will help to inform us on architectural choices for optimizing coherence and coupling in next-generation quantum annealers.

APPENDIX E: RESIDUAL COUPLING WITH COUPLER BIASED "OFF"

Here, we describe the technique that we use to place an upper bound on any residual coupling when the coupler is nominally biased to provide zero coupling ($f_C = 0.402$). As we illustrate in Fig. 11, we observe no avoided crossing in spectroscopy, allowing us to bound any nonzero residual coupling to <220 kHz, a limit determined by the resolution in f_A set by our bias-current source. For each value of f_A, the frequency of qubit A is determined by fitting the spectroscopy trace to a Gaussian function. Qubit B is biased on degeneracy, and its frequency is precisely determined through Ramsey spectroscopy.

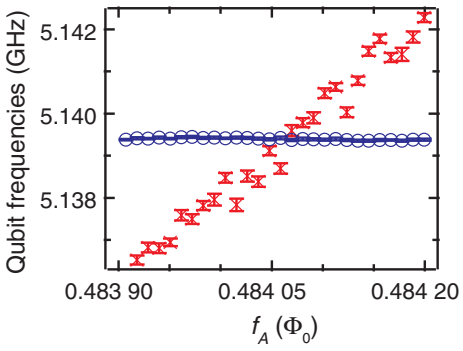

FIG. 11. Zero coupling. Detailed data for the qubit-level crossing with the coupler nominally biased for zero coupling ($f_C = 0.5$). Red hourglasses: Qubit A. Blue circles: Qubit B.

[1] A. Finnila, M. Gomez, C. Sebenik, C. Stenson, and J. Doll, Quantum annealing: A new method for minimizing multidimensional functions, Chem. Phys. Lett. **219**, 343 (1994).

[2] T. Kadowaki and H. Nishimori, Quantum annealing in the transverse Ising model, Phys. Rev. E **58**, 5355 (1998).

[3] J. Brooke, D. Bitko, T. F. Rosenbaum, and G. Aeppli, Quantum annealing of a disordered magnet, Science **284**, 779 (1999).

[4] E. Farhi, J. Goldstone, S. Gutmann, J. Lapan, A. Lundgren, and D. Preda, A quantum adiabatic evolution algorithm applied to random instances of an NP-complete problem, Science **292**, 472 (2001).

[5] A. Lucas, Ising formulations of many NP problems, Front. Phys. **2**, 5 (2014).

[6] T. F. Rønnow, Z. Wang, J. Job, S. Boixo, S. V. Isakov, D. Wecker, J. M. Martinis, D. A. Lidar, and M. Troyer, Defining and detecting quantum speedup, Science **345**, 420 (2014).

[7] S. Boixo, T. F. Ronnow, S. V. Isakov, Z. Wang, D. Wecker, D. A. Lidar, J. M. Martinis, and M. Troyer, Evidence for quantum annealing with more than one hundred qubits, Nat. Phys. **10**, 218 (2014).

[8] T. Lanting *et al.*, Entanglement in a Quantum Annealing Processor, Phys. Rev. X **4**, 021041 (2014).

[9] T. Albash, I. Hen, F. M. Spedalieri, and D. A. Lidar, Reexamination of the evidence for entanglement in a quantum annealer, Phys. Rev. A **92**, 062328 (2015).

[10] H. G. Katzgraber, F. Hamze, Z. Zhu, A. J. Ochoa, and H. Munoz-Bauza, Seeking Quantum Speedup through Spin Glasses: The Good, the Bad, and the Ugly, Phys. Rev. X **5**, 031026 (2015).

[11] S. Isakov, I. Zintchenko, T. Rnnow, and M. Troyer, Optimised simulated annealing for Ising spin glasses, Comput. Phys. Commun. **192**, 265 (2015).
[12] S. Boixo, V. N. Smelyanskiy, A. Shabani, S. V. Isakov, M. Dykman, V. S. Denchev, M. H. Amin, A. Y. Smirnov, M. Mohseni, and H. Neven, Computational multiqubit tunnelling in programmable quantum annealers, Nat. Commun. **7**, 10327 (2016).
[13] V. S. Denchev, S. Boixo, S. V. Isakov, N. Ding, R. Babbush, V. Smelyanskiy, J. Martinis, and H. Neven, What is the Computational Value of Finite-Range Tunneling?, Phys. Rev. X **6**, 031015 (2016).
[14] S. Mandrà, Z. Zhu, W. Wang, A. Perdomo-Ortiz, and H. G. Katzgraber, Strengths and weaknesses of weak-strong cluster problems: A detailed overview of state-of-the-art classical heuristics versus quantum approaches, Phys. Rev. A **94**, 022337 (2016).
[15] S. Bravyi, D. P. Divincenzo, R. Oliveira, and B. M. Terhal, The complexity of stoquastic local Hamiltonian problems, Quantum Inf. Comput. **8**, 361 (2008).
[16] R. Harris, J. Johansson, A. J. Berkley, M. W. Johnson, T. Lanting, S. Han, P. Bunyk, E. Ladizinsky, T. Oh, I. Perminov, E. Tolkacheva, S. Uchaikin, E. M. Chapple, C. Enderud, C. Rich, M. Thom, J. Wang, B. Wilson, and G. Rose, Experimental demonstration of a robust and scalable flux qubit, Phys. Rev. B **81**, 134510 (2010).
[17] P. I. Bunyk, E. M. Hoskinson, M. W. Johnson, E. Tolkacheva, F. Altomare, A. J. Berkley, R. Harris, J. P. Hilton, T. Lanting, A. J. Przybysz, and J. Whittaker, Architectural considerations in the design of a superconducting quantum annealing processor, IEEE Trans. Appl. Supercond. **24**, 1 (2014).
[18] D. Kafri, C. Quintana, Y. Chen, A. Shabani, J. M. Martinis, and H. Neven, Tunable inductive coupling of superconducting qubits in the strongly nonlinear regime, Phys. Rev. A **95**, 052333 (2017).
[19] J. E. Mooij, T. P. Orlando, L. Levitov, L. Tian, C. H. van der Wal, and S. Lloyd, Josephson persistent-current qubit, Science **285**, 1036 (1999).
[20] T. P. Orlando, J. E. Mooij, L. Tian, C. H. van der Wal, L. S. Levitov, S. Lloyd, and J. J. Mazo, Superconducting persistent-current qubit, Phys. Rev. B **60**, 15398 (1999).
[21] B. L. T. Plourde, J. Zhang, K. B. Whaley, F. K. Wilhelm, T. L. Robertson, T. Hime, S. Linzen, P. A. Reichardt, C.-E. Wu, and J. Clarke, Entangling flux qubits with a bipolar dynamic inductance, Phys. Rev. B **70**, 140501 (2004).
[22] A. M. van den Brink, A. J. Berkley, and M. Yalowsky, Mediated tunable coupling of flux qubits, New J. Phys. **7**, 230 (2005).
[23] A. O. Niskanen, K. Harrabi, F. Yoshihara, Y. Nakamura, and J. S. Tsai, Spectroscopy of three strongly coupled flux qubits, Phys. Rev. B **74**, 220503 (2006).
[24] S. H. W. van der Ploeg, A. Izmalkov, A. M. van den Brink, U. Hübner, M. Grajcar, E. Il'ichev, H.-G. Meyer, and A. M. Zagoskin, Controllable Coupling of Superconducting Flux Qubits, Phys. Rev. Lett. **98**, 057004 (2007).
[25] V. Zakosarenko, N. Bondarenko, S. H. W. van der Ploeg, A. Izmalkov, S. Linzen, J. Kunert, M. Grajcar, E. Il'ichev, and H.-G. Meyer, Realization of a classical counterpart of a scalable design for adiabatic quantum computation, Appl. Phys. Lett. **90**, 022501 (2007).
[26] R. Harris, A. J. Berkley, M. W. Johnson, P. Bunyk, S. Govorkov, M. C. Thom, S. Uchaikin, A. B. Wilson, J. Chung, E. Holtham, J. D. Biamonte, A. Y. Smirnov, M. H. S. Amin, and A. Maassen van den Brink, Sign- and Magnitude-Tunable Coupler for Superconducting Flux Qubits, Phys. Rev. Lett. **98**, 177001 (2007).
[27] S. Ashhab, A. O. Niskanen, K. Harrabi, Y. Nakamura, T. Picot, P. C. de Groot, C. J. P. M. Harmans, J. E. Mooij, and F. Nori, Interqubit coupling mediated by a high-excitation-energy quantum object, Phys. Rev. B **77**, 014510 (2008).
[28] R. Harris, T. Lanting, A. J. Berkley, J. Johansson, M. W. Johnson, P. Bunyk, E. Ladizinsky, N. Ladizinsky, T. Oh, and S. Han, Compound Josephson-junction coupler for flux qubits with minimal crosstalk, Phys. Rev. B **80**, 052506 (2009).
[29] M. S. Allman, F. Altomare, J. D. Whittaker, K. Cicak, D. Li, A. Sirois, J. Strong, J. D. Teufel, and R. W. Simmonds, rf-SQUID-Mediated Coherent Tunable Coupling between a Superconducting Phase Qubit and a Lumped-Element Resonator, Phys. Rev. Lett. **104**, 177004 (2010).
[30] M. S. Allman, J. D. Whittaker, M. Castellanos-Beltran, K. Cicak, F. da Silva, M. P. DeFeo, F. Lecocq, A. Sirois, J. D. Teufel, J. Aumentado, and R. W. Simmonds, Tunable Resonant and Nonresonant Interactions between a Phase Qubit and *LC* Resonator, Phys. Rev. Lett. **112**, 123601 (2014).
[31] Y. Chen *et al.*, Qubit Architecture with High Coherence and Fast Tunable Coupling, Phys. Rev. Lett. **113**, 220502 (2014).
[32] F. Yan, S. Gustavsson, A. Kamal, J. Birenbaum, A. P. Sears, D. Hover, T. J. Gudmundsen, D. Rosenberg, G. Samach, S. Weber, J. L. Yoder, T. P. Orlando, J. Clarke, A. J. Kerman, and W. D. Oliver, The flux qubit revisited to enhance coherence and reproducibility, Nat. Commun. **7**, 12964 (2016).
[33] C. M. Quintana *et al.*, Observation of Classical-Quantum Crossover of $1/f$ Flux Noise and Its Paramagnetic Temperature Dependence, Phys. Rev. Lett. **118**, 057702 (2017).
[34] A. Blais, R.-S. Huang, A. Wallraff, S. M. Girvin, and R. J. Schoelkopf, Cavity quantum electrodynamics for superconducting electrical circuits: An architecture for quantum computation, Phys. Rev. A **69**, 062320 (2004).
[35] S. Gustavsson, F. Yan, G. Catelani, J. Bylander, A. Kamal, J. Birenbaum, D. Hover, D. Rosenberg, G. Samach, A. P. Sears, S. J. Weber, J. L. Yoder, J. Clarke, A. J. Kerman, F. Yoshihara, Y. Nakamura, T. P. Orlando, and W. D. Oliver, Suppressing relaxation in superconducting qubits by quasiparticle pumping, Science **354**, 1573 (2016).
[36] In our previous work [32], we determined that $\alpha = 0.9$ for capacitively shunted flux qubits with (10×10)-μm^2 loops produced using our fabrication process. Here, we choose to use $\alpha = 0.91$ in order achieve a good fit to our coherence data, as we discuss in Appendix D.
[37] A. J. Kerman and W. D. Oliver, High-Fidelity Quantum Operations on Superconducting Qubits in the Presence of Noise, Phys. Rev. Lett. **101**, 070501 (2008).
[38] A. J. Kerman (to be published).

[39] M. H. Devoret and J. M. Martinis, in *Quantum Entanglement and Information Processing*, Proceedings of Les Houches Summer School, Session LXXIX, edited by J.-M. Raimond, J. Dalibard, and D. Esteve (Elsevier, New York, 2003), pp. 443–485.

[40] This 2×2 inductance matrix is appropriate in the limit of small island capacitance of the node connecting the three inductors. In this limit, independent phase fluctuations of this node can be neglected, and the circuit can be described by only two canonical phase variables with a 2×2 inductance matrix.

[41] G. Johansson, L. Tornberg, and C. M. Wilson, Fast quantum limited readout of a superconducting qubit using a slow oscillator, Phys. Rev. B **74**, 100504 (2006).

[42] L. Tornberg and G. Johansson, Dispersive charge and flux qubit readout as a quantum measurement process, J. Low Temp. Phys. **146**, 227 (2007).

[43] M. A. Sillanpää, T. Lehtinen, A. Paila, Y. Makhlin, L. Roschier, and P. J. Hakonen, Direct Observation of Josephson Capacitance, Phys. Rev. Lett. **95**, 206806 (2005).

[44] T. Duty, G. Johansson, K. Bladh, D. Gunnarsson, C. Wilson, and P. Delsing, Observation of Quantum Capacitance in the Cooper-Pair Transistor, Phys. Rev. Lett. **95**, 206807 (2005).

[45] J. I. Colless, A. C. Mahoney, J. M. Hornibrook, A. C. Doherty, H. Lu, A. C. Gossard, and D. J. Reilly, Dispersive Readout of a Few-Electron Double Quantum Dot with Fast rf Gate Sensors, Phys. Rev. Lett. **110**, 046805 (2013).

[46] K. D. Petersson, G. Smith, D. Anderson, P. Atkinson, G. A. C. Jones, and D. A. Ritchie, Charge and spin state readout of a double quantum dot coupled to a resonator, Nano Lett. **10**, 2789 (2010).

[47] S. Ilani, L. A. K. Donev, M. Kindermann, and P. L. McEuen, Measurement of the quantum capacitance of interacting electrons in carbon nanotubes, Nat. Phys. **2**, 687 (2006).

[48] L. I. Glazman, I. M. Ruzin, and B. I. Shklovskii, Quantum transport and pinning of a one-dimensional Wigner crystal, Phys. Rev. B **45**, 8454 (1992).

[49] M. M. Fogler, Ground-State Energy of the Electron Liquid in Ultrathin Wires, Phys. Rev. Lett. **94**, 056405 (2005).

[50] L. Latessa, A. Pecchia, A. Di Carlo, and P. Lugli, Negative quantum capacitance of gated carbon nanotubes, Phys. Rev. B **72**, 035455 (2005).

[51] Note that a general treatment will also include the effective inductance of qubit A $L_{\mathrm{eff}}^{(A)}$, but for the device parameters presented here, $L_{\mathrm{eff}}^{(A)} \gg L_{\mathrm{eff}}^{(C)}$ and, therefore, has a negligible effect on qubit B.

[52] Note that our definition for $S_\lambda(\omega)$ differs by a factor of 2π from the expression used in Ref. [53], but for the case of $\gamma = 1$, our definitions of A_λ are equivalent. Also note that our definition of $S_\lambda(\omega)$ is double sided and, thus, differs by a factor of 2 from the single-sided spectral density used in Ref. [54].

[53] J. Bylander, S. Gustavsson, F. Yan, F. Yoshihara, K. Harrabi, G. Fitch, D. G. Cory, Y. Nakamura, J.-S. Tsai, and W. D. Oliver, Noise spectroscopy through dynamical decoupling with a superconducting flux qubit, Nat. Phys. **7**, 565 (2011).

[54] D. Sank, R. Barends, R. C. Bialczak, Y. Chen, J. Kelly, M. Lenander, E. Lucero, M. Mariantoni, A. Megrant, M. Neeley, P. J. J. O'Malley, A. Vainsencher, H. Wang, J. Wenner, T. C. White, T. Yamamoto, Y. Yin, A. N. Cleland, and J. M. Martinis, Flux Noise Probed with Real Time Qubit Tomography in a Josephson Phase Qubit, Phys. Rev. Lett. **109**, 067001 (2012).

[55] In reality, when biased away from coupler degeneracy, the qubit dephasing is somewhat nonexponential. However, it is difficult to quantify the nonexponential decay using the existing data, and any nonexponential corrections to $\Gamma_{N,\mathrm{other}}$ will have only a small impact on our estimation of A_{Φ_C}.

[56] T. Lanting, A. J. Berkley, B. Bumble, P. Bunyk, A. Fung, J. Johansson, A. Kaul, A. Kleinsasser, E. Ladizinsky, F. Maibaum, R. Harris, M. W. Johnson, E. Tolkacheva, and M. H. S. Amin, Geometrical dependence of the low-frequency noise in superconducting flux qubits, Phys. Rev. B **79**, 060509 (2009).